



@2019 IOP. Access to this work was provided by the University of Maryland, Baltimore County (UMBC) ScholarWorks@UMBC digital repository on the Maryland Shared Open Access (MD-SOAR) platform.

Please provide feedback

Please support the ScholarWorks@UMBC repository by emailing scholarworks-group@umbc.edu and telling us what having access to this work means to you and why it's important to you. Thank you.



Developing the Physical Understanding of Intermediate Polars: An X-Ray Study of TV Col and V2731 Oph

R. Lopes de Oliveira^{1,2,3,4}  and K. Mukai^{2,5} 

¹ X-ray Astrophysics Laboratory, NASA Goddard Space Flight Center, Greenbelt, MD 20771, USA; rlopes@ufs.br

² Center for Space Science and Technology, University of Maryland, Baltimore County, 1000 Hilltop Circle, Baltimore, MD 21250, USA

³ Departamento de Física, Universidade Federal de Sergipe, Av. Marechal Rondon, S/N, 49000-000 São Cristóvão, SE, Brazil

⁴ Observatório Nacional, Rua Gal. José Cristino 77, 20921-400, Rio de Janeiro, RJ, Brazil

⁵ CRESST II and X-ray Astrophysics Laboratory, NASA Goddard Space Flight Center, Greenbelt, MD 20771, USA

Received 2019 March 14; revised 2019 June 17; accepted 2019 June 18; published 2019 August 2

Abstract

The X-rays in intermediate polars (IPs) originate in a compact region near the surface of a magnetic white dwarf (WD) and interact with the complex environment surrounding the emission region. Here we report a case study of two IPs, TV Col and V2731 Oph, with selected archival X-ray observations (*NuSTAR*, *Swift*, *Suzaku*, and *XMM-Newton*). For TV Col, we were successful in simultaneously accounting for the primary X-rays, the secondary X-rays due to Compton scattering and fluorescence, and the effects of local absorbers. In this case, we were able to demonstrate that the shock height is small, based on the high reflection amplitude; hence, the maximum temperature of the post-shock region can be used to derive the WD mass of $0.735 \pm 0.015 M_{\odot}$. Despite the high specific accretion rate required to explain the small shock height, we do not detect any spin modulation in our *NuSTAR* data, consistent with the modest amount of complex absorption seen spectroscopically. We argue that our results are robust because they are based on the joint temporal–spectral analysis of broadband X-ray data. The spectrum of V2731 Oph is more highly absorbed. Through our analysis of the *Suzaku* data, we present a spectral model with nitrogen overabundance without the previously claimed soft blackbody that should be further explored. We have been unable to constrain the reflection amplitude for V2731 Oph; this and the detection of spin modulation above 10 keV suggest that it may have a tall shock. Hence, we only derive a lower limit to the mass of its WD ($>0.9 M_{\odot}$).

Key words: novae, cataclysmic variables – stars: individual (TV Col, V2731 Oph) – ultraviolet: stars – X-rays: binaries

1. Introduction

Intermediate polars (IPs) are a subgroup of cataclysmic variables (CVs) in which a moderately magnetic (10^{5-7} G) white dwarf (WD) accretes matter via Roche-lobe overflow from a companion, usually a low-mass star on or near the main sequence. An accretion disk is usually formed, and its inner part is truncated by the magnetic field, which channels the gas in accretion columns toward the magnetic poles of the WD. Strong shocks are formed in the columns, heating up the gas to a high temperature defined in the first order by the depth of the gravitational potential well of the WD ($kT \propto M_{\text{WD}}/R_{\text{WD}}$). The shocked gas subsequently settles onto the WD surface as it is cooled by radiating X-rays and cyclotron emission. Thus, the X-ray emission is intrinsically multitemperature in nature.

Information on the accretion geometry and WD mass is encoded in the intrinsic emission and its subsequent interaction with its surroundings. The observed radiation in IPs has a significant contribution from X-ray photons that have interacted with the environment, including the stellar surface of the WD itself, the accretion column, the accretion disk, and any circumstellar medium that might exist. Part of the interacting X-rays suffers photoelectric absorption inducing a deficit in the observed X-rays that is more pronounced for softer photons. Another part is reflected and results in excess in the continuum around 10–30 keV as a Compton hump and in fluorescent emission lines, notably the Fe K line at 6.4 keV. The description of both components, absorption and reflection, is necessary for an in-depth understanding of the accretion geometry and characteristics of the intrinsic X-rays, which

can also lead to the determination of the WD mass. This task requires wide-bandpass spectroscopy covering both soft and hard X-rays—especially because the partial-covering absorption, expected in IPs due to their complex environment, can have a similar effect on the spectral shape around the Fe K edge as reflection.

The advent of imaging hard X-ray observations using *NuSTAR* has allowed the detailed investigation of X-ray spectra of IPs, including both absorption and reflection (Mukai et al. 2015). While other recent papers have concentrated on deriving the WD mass using hard X-ray spectroscopy (Shaw et al. 2018), including the effects of tall shocks and a small inner radius of the disk (Suleimanov et al. 2019), concerns remain that such investigations can be compromised if inadequate attention is paid to the complex interplay of absorption, reflection, and intrinsic spectral shape. Here we present our detailed analysis of wideband X-ray spectra of two IPs, TV Col and V2731 Oph, to test the potential degeneracy in spectral analysis results. We also follow Mukai et al. (2015) in analyzing the hard X-ray spin modulation as a method to break the degeneracy.

2. The Targets

According to the *Gaia* DR2 parallax, TV Col is at a distance of 513_{-3}^{+4} pc (Gaia Collaboration et al. 2016, 2018). The system has been investigated with many X-ray observatories since its first detection with the *Ariel V* satellite (2A 0526-328; Cooke et al. 1978). *EXOSAT* observations (~ 2 –10 keV) revealed it to be an absorbed hard X-ray emitter with flux modulated at

1911 s, interpreted as the WD spin period (Schrijver et al. 1987). Based on the energy-dependent pulse profile from *EXOSAT* data, Norton & Watson (1989) argued for the presence of a complex absorption structure that could be explained by a partial-covering absorption. The spin period was refined to 1909.7 ± 2.5 s by Rana et al. (2004) from a nearly sinusoidal modulation by using *RXTE*, *ROSAT*, and *ASCA* data, which also showed the 5.5 hr orbital modulation. The authors also claimed the presence of a strong attenuation of the X-rays and signals of partial-covering absorption from hardness ratio variations and spin modulation decreasing with energy. Broadband *RXTE* spectra (Proportional Counter Array and High-Energy X-Ray Timing Experiment; ~ 3 –100 keV) confirmed that TV Col is a hard, thermal, X-ray source presenting a clear Fe K α complex (Suleimanov et al. 2005). A single-temperature thermal fit of the high-energy *Neil Gehrels Swift Observatory* (*Swift*)/BAT (15–195 keV) data resulted in a temperature of $kT = 21.6 \pm 2.4$ keV (Brunschweiler et al. 2009). An analysis of the *Suzaku* data in the 3–50 keV range, with the inclusion of a partial-covering absorber, indicated a shock temperature $kT = 45.7_{-9.1}^{+16.6}$ keV in a plasma with a subsolar abundance ($0.49 Z_{\odot}$; Yuasa et al. 2010).

At a distance of 2300_{-270}^{+330} pc (Gaia Collaboration et al. 2016, 2018), V2731 Oph is the hardest X-ray-luminous IP known ($\log L_{(X:14-195 \text{ keV})} > 33.9$ for $d > 1$ kpc; Pretorius & Mukai 2014). First investigated in X-rays by de Martino et al. (2008) using *XMM-Newton* and *International Gamma-Ray Astrophysics Laboratory* (*INTEGRAL*) observations, V2731 Oph was revealed to have a complex X-ray emission. The investigation in broadband energy (0.2–100 keV) showed two optically thin plasma components, one cold ($kT \sim 0.2$ keV) and another hot ($kT \sim 60$ keV), with an additional contribution of a hot blackbody ($kT \sim 90$ eV). The intrinsic X-rays suffer the effects of a complex (local) distribution of cold intervening material plus a warm absorber, the latter being suggested by an OVII absorption edge at 0.74 keV. As with TV Col, the pulse modulation for V2731 Oph depends on the energy. In the case of V2731 Oph, the X-rays are spin-modulated (128.02 ± 0.02 s), while UV emission is unmodulated at the 3σ level (de Martino et al. 2008).

More recently, both TV Col and V2731 Oph were observed with *NuSTAR* and investigated in the 3–50 keV band by Hailey et al. (2016) in the context of the X-ray emission of the Galactic center. We revisit those observations for a more in-depth investigation of the X-ray reflection and absorption in these systems and, consequently, the characterization of IPs in general. We include in the investigation the *Swift*/XRT observation carried out during the *NuSTAR* observation of TV Col, and we show that the inclusion of soft X-rays is crucial to disentangle the effects of absorption and reflection in IP systems. For the same reason, we discuss the constraints imposed by previous *XMM-Newton*, *Suzaku*, and *Swift* observations of V2731 Oph. Also, contrary to the previous study with *NuSTAR* data (Hailey et al. 2016), we fit the spectra using the cooling-flow model that takes into account the ionized Fe K lines.

3. Observations and Data Reduction

Details of the X-ray observations used in this investigation are given in Table 1. The *NuSTAR* satellite observed TV Col on 2014 May 11 for 49.7 ks (ObsID 30001020002). The system was also simultaneously observed by *Swift* for ~ 1.9 ks on 2014 May 12 (ObsID 00080734001). For the first time, we explored

Table 1
Journal of X-Ray Observations

TV Col	ObsID	Date	Exposure
<i>Swift</i>	00035282001	2007 Mar 30	7 ks
	00035282002	2007 Apr 23	0.8 ks
	00037150002	2007 Dec 21	19.4 ks
	00037150003	2007 Dec 27	4.6 ks
	00037150005	2008 Jan 14	5.3 ks
	00080734001	2014 May 12	1.9 ks
<i>NuSTAR</i>	30001020002	2014 May 11	49.7 ks
V2731 Oph			
<i>XMM-Newton</i>	0302100201	2005 Aug 29	13.5 ks
<i>Swift</i>	00035086002	2007 Feb 23	12.8 ks
<i>Suzaku</i>	403026010	2009 Feb 16	32.9 ks
<i>NuSTAR</i>	30001019002	2014 May 14	50 ks

Note. The covered energy range was 0.3–10 keV for the *XMM-Newton*, *Swift*, and *Suzaku* satellites; for *NuSTAR*, it was 3–60 keV for TV Col and 3–75 keV (or 20–75 keV; see text) for V2731 Oph.

the corresponding *NuSTAR* FPMA/FPMB and *Swift*/XRT data sets to carry out consistent wideband spectroscopy from 0.35 to 75 keV. We also investigated five other *Swift*/XRT observations in order to obtain clues on the spectral variations of the source.

We investigated V2731 Oph using a *NuSTAR* observation carried out for ~ 50 ks on 2014 May 14 (ObsID 30001019002), for which there is no contemporaneous X-ray observation with another satellite. However, we used archival observations, namely, *XMM-Newton*/EPIC (2005 August 29, 13.5 ks; ObsID 0302100201), *Suzaku* (2009 February 16, 32.9 ks; ObsID 403026010), and the longest *Swift* (2007 February 23, 12.8 ks; ObsID 00035086002) observations in order to evaluate the source in soft X-rays and discuss implications for the description of the system.

The data reduction followed standard procedures with the appropriated tools (with HEASOFT-v6.22 for the *NuSTAR*, *Swift*, and *Suzaku* data and SAS-v16.1.0 for the *XMM-Newton* data) with the latest calibration files that were available in 2017 November. We use different extraction regions for the *NuSTAR* modules, FPMA and FPMB, based on their individual images to accommodate the relative astrometric offset between them.

All spectra from both TV Col and V2731 Oph were binned such that each energy bin contains at least 25 counts, except for the *Swift*/XRT data of TV Col. For those data, a 5 count limit was adopted, as enforcing 25 counts per bin, making Gaussian errors a reasonable approximation, would have meant too few spectral bins for the spectrum to be useful. Spectral fits were done with Xspec v12.9.1 m by using the χ^2 as fit and test statistics but applying the C statistic for the fit in all cases in which the *Swift*/XRT data of TV Col were investigated—as it is appropriate to low count per energy bin, following the deviation from Gaussian to Poisson data.

4. X-Ray Spectroscopy

Throughout this work, we use XSPEC and models available within it to carry out modeling of *XMM-Newton*, *Swift*, *Suzaku*, and *NuSTAR* X-ray spectra. Two optically thin thermal models were used: a single-temperature APEC model and a

Table 2
Spectral Models

Target	Model	Description
TV Col	M1	CONSTANT*PHABS*[(APEC or MKCFLOW)+GAUSS]
	M2	CONSTANT*PHABS*[REFLECT*(APEC or MKCFLOW)+GAUSS]
	M3	CONSTANT*PHABS*PWAB*[(APEC or MKCFLOW)+GAUSS]
	M4	CONSTANT*PHABS*PWAB*[REFLECT*(APEC or MKCFLOW)+GAUSS]
	M5	CONSTANT*PHABS*PWAB*[REFLECT*(APEC or MKCFLOW)+(APEC or BBODY)+GAUSS]
V2731 Oph	M6	CONSTANT*PHABS*PWAB*EDGE*(APEC+MKCFLOW+BBODY+GAUSSIAN)
	M7	CONSTANT*PHABS*PWAB*EDGE*(APEC+REFLECT*MKCFLOW+BBODY+GAUSSIAN)
	M8	CONSTANT*PHABS*PWAB*EDGE*(VAPEC+VMCFLOW+GAUSSIAN)
	M9	CONSTANT*PHABS*PWAB*EDGE*(VAPEC+VMCFLOW+BBODY+GAUSSIAN+GAUSSIAN+GAUSSIAN)

multitemperature cooling-flow model with MKCFLOW, also based on APEC (with the *switch* parameter equal to 2), which is model M1. In addition, an optically thick blackbody model, BBODY, was included as necessary. The abundance table applied in both optically thin thermal models was that of Asplund et al. (2009). The redshift required by construction in the MKCFLOW model cannot be zero. It was assumed to be 8.5867×10^{-8} for TV Col and 5.367×10^{-7} for V2731 Oph, as estimated from the *Gaia* DR2 distances (513_{-5}^{+4} and 2300_{-270}^{+330} pc, respectively; Gaia Collaboration et al. 2016, 2018) and standard cosmological values of XSPEC. The low temperature of the MKCFLOW was fixed to the minimum value allowed by the model ($kT = 80.8$ eV).

The interaction of the radiation with matter was accounted for by the following models. For the photoelectric absorption by cold matter, we use both the single-absorber PHABS and the complex-absorber *pwab* (Done & Magdziarz 1998) components. The usual partial-covering absorber models (either the PCFABS multiplicative model or the PARTCOV convolution model combined with any absorption model) represent two lines of sight, one with and one without an intervening absorber. However, the absorption in the pre-shock accretion columns of magnetic CVs requires a model with a continuous distribution of covering fraction as a function of column height. Done & Magdziarz (1998) developed *pwab* to represent this situation, in which the covering fraction is assumed to be a power-law function of the column (β index, from a minimum ($N_{H,\min}$) to a maximum ($N_{H,\max}$) equivalent hydrogen columns). An EDGE component was used to account for a warm absorber, only necessary in the case of V2731 Oph, associated with the O VII absorption edge at 0.74 keV. The REFLECT model was applied when investigating the reflection of X-rays in the systems, in all cases keeping the (unconstrained) inclination angle (i) of the reflecting surface equal to the default value in the model, such that $\cos(i)$ is equal to 0.45.

The GAUSS model was used to describe the 6.4 keV fluorescence iron line, with the line energy (E_c) and width (σ) fixed to 6.4 and 0.01 keV, respectively. An energy-independent multiplicative factor, the CONSTANT model, was included to account for the cross-calibration uncertainties of the different instruments (namely, the impact on normalization in spectral modeling) when two or more spectra were used in simultaneous fits. CONSTANT also helps with source flux variability, since the observations are not all simultaneous. All parameters cited above as being fixed were not constrained when they were allowed to vary freely during the fit.

We notice that the statistical significance for the *NuSTAR* and *Swift* simultaneous fit of the TV Col spectra is biased to the

NuSTAR data, and thus the visual check was crucial to choose between the models. For TV Col, we started with the simplest model based on single absorption for the two optically thin thermal models cited above (APEC and MKCFLOW; M1), then added the reflection model (M2), replaced the reflection model with the partial-covering model (M3), and finally, used both partial-covering and reflection models (M4). In all cases, a Gaussian line at 6.4 keV was added to describe the Fe K α fluorescence feature. Some *Swift* spectra of TV Col presented an excess in soft X-rays that was accounted for as an additional thermal component (M5). Thus, the four initial models are a subgroup of M5, as described in Table 2. For V2731 Oph, the starting point was the result of de Martino et al. (2008) from *XMM-Newton* and *INTEGRAL* data. Finally, the model applied to the system was CONSTANT*PHABS*PWAB*EDGE*(MKCFLOW+APEC+BBODY+GAUSSIAN). Table 2 summarizes the models.

When using the REFLECT component, we extended the energy range over which the model is calculated to 100 keV, because photons with energies above the instrumental coverage can be Compton down-scattered to the energy range which is covered by the instrument (command ENERGIES EXTEND HIGH 100.0, in XSPEC). The output spectrum was limited to 80 keV to speed up the calculation of the spectrum (command XSET REFLECT_MAX_E 80.0 in XSPEC).

4.1. TV Col

TV Col is among the brightest IPs in the hard X-ray band (Pretorius & Mukai 2014). Its X-rays are due to optically thin, thermal plasma, as supported by the strong Fe K line complex. Because of its Galactic latitude of $-30^{\circ}6$ and distance of 513_{-5}^{+4} pc, most of the interstellar medium (ISM) in its direction is between us and TV Col. However, the system occupies a relatively unobscured part of the Galaxy with an integrated HI column density estimate of only $\sim 2.39 \times 10^{20} \text{ cm}^{-2}$ (Kalberla et al. 2005). Thus, the X-rays from TV Col are only slightly affected by the ISM, and any absorption we measure is due to local contributions. These circumstances make it an ideal target for a detailed study of intrinsic absorbers in the system and therefore of reflection effects. We base our spectral analysis on these two premises and proceed from the simplest model to more complex ones until satisfactory fits are obtained.

4.1.1. Broadband Spectroscopy from Simultaneous *Swift* and *NuSTAR* Observations

We first investigate TV Col by simultaneously fitting the contemporaneous *NuSTAR* (FPMA + FPMB; 3–60 keV) and *Swift*/XRT spectra (0.35–10 keV; Section 3) that together

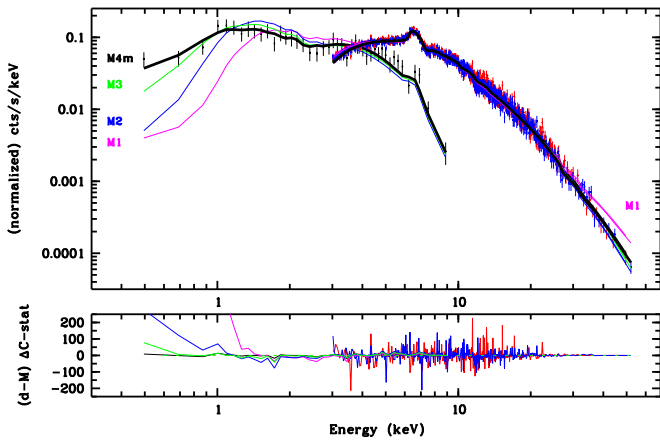


Figure 1. TV Col: *NuSTAR*/FPMA and *Swift*/XRT spectra fitted with models M1 (magenta), M2 (blue), M3 (green), and M4_m (black; see text for further details). The lower panel shows the residual with respect to M4_m.

covered the wide energy range from 0.35 to 60 keV. The iron line complex (via *NuSTAR*) and the soft part of the spectrum (via XRT) were always included, which played a key role in disentangling the models.

A thermal model affected by a single absorption component (M1) with either APEC and MKCFLOW does not describe the data. It fails in the description of the continuum, especially at low energies (see Figure 1). However, this simple model immediately reveals the presence of a complex absorption pattern in the system. This model underestimates the flux for $E < 1.5$ keV appreciably, showing that the absorber with a high column density that is required to explain the spectral shape at higher energies absorbs too many soft photons. Similar results were obtained when including the reflection component (M2). The fit was substantially improved when the reflection component was replaced by the partial-covering model (M3) but still yielded an unacceptable description for energies up to ~ 6 keV, below which the model oscillates between underestimating and overestimating the flux. Finally, the reflection was added to M3 by using the M4 model. This model significantly improved the fit over the whole spectrum, as described below.

Contrary to the first three models, M4 describes the continuum from 0.35 to 60 keV (see Figure 1). The distinction between model M4 using APEC (M4_a) or MKCFLOW (M4_m) comes from the description of the Fe K complex and the surrounding continuum. While the spectral fit from APEC substantially underestimates the flux from the ionized Fe XXV line, the MKCFLOW model describes both it and the Fe XXVI lines and results in a better description of the continuum at ~ 4 –8 keV—M4_m, the assumed model for TV Col in this work, resulting in a χ^2_ν of 0.95 for 1007 degrees of freedom.

We present the best-fit parameters for M4_m in Table 3. The equivalent hydrogen column from the PHABS model is constrained to be less than $3.0 \times 10^{20} \text{ cm}^{-2}$ such that any intrinsic absorption would be mitigated by the effect of the dominant local partial-covering absorber. Thus, although the values of all parameters are still mutually consistent at 1σ , we assume a conservative upper limit by fixing the column value to the total Galactic column in the direction of TV Col ($2.39 \times 10^{20} \text{ cm}^{-2}$; Kalberla et al. 2005). This procedure improves the determination of the absorption derived from the partial-covering absorption pwab model, resulting in

Table 3

TV Col: Best-fit Spectral Parameters from the Simultaneous Fit of the Contemporaneous *NuSTAR* (FPMA and FPMB) and *Swift*/XRT Spectra from the Best-fit M4_m Model (as in Table 2)

Component	Parameter	Value
PHABS	N_{H} (10^{22} cm^{-2})	0.0239 ^(*)
	$N_{\text{H,min}}$ (10^{22} cm^{-2})	10^{-7} (*)
	$N_{\text{H,max}}$ (10^{22} cm^{-2})	$10.5^{+1.7}_{-0.8}$
	β	$-0.41^{+0.03}_{-0.04}$
REFLECT	rel _{refl}	$0.88^{+0.13}_{-0.13}$
	cos(i)	0.45 ^(*)
MKCFLOW	kT_{low} (keV)	0.0808 ^(*)
	kT_{max} (keV)	$31.0^{+1.1}_{-1.1}$
	Z ($\times Z_{\odot}$)	$0.49^{+0.04}_{-0.04}$
	Redshift	1.197×10^{-7} (*)
	Switch	2
	$\chi^2_\nu/\text{d.o.f.}$	0.95/1007

Note. (*) fixed parameter (see text).

$N_{\text{H,max}} = 1.05^{+0.17}_{-0.08} \times 10^{23} \text{ cm}^{-2}$ and $\beta = -0.41^{+0.03}_{-0.04}$. The primary source of X-rays is a high-temperature plasma with an abundance of 0.49 ± 0.04 times the solar values, cooling down from a maximum temperature kT of 31.0 ± 1.1 keV. If we take this as the measurement of the gravitational potential at the surface of the WD, then its mass is $0.735 \pm 0.015 M_{\odot}$ (following Aizu 1973). Our subsequent analysis justifies this assumption, as we discuss in Section 6.2.

We find that the reflection of the primary X-rays makes a nonnegligible contribution to the observed X-rays. According to the best-fit model (M4_m), the reflection amplitude is constrained to be $0.88^{+0.13}_{-0.13}$. The reflection accounts for about 16% of a total unabsorbed flux of $\sim 1.37 \times 10^{-10} \text{ erg s}^{-1} \text{ cm}^{-2}$ at 0.3–75 keV, increasing to 30% of a total of $\sim 5.3 \times 10^{-11} \text{ erg s}^{-1} \text{ cm}^{-2}$ at 10–50 keV (and 7.6% of $\sim 7.9 \times 10^{-11} \text{ erg s}^{-1} \text{ cm}^{-2}$ at 0.3–10 keV). On 2014 May 11/12, TV Col was observed with a luminosity of $4.3 \times 10^{33} \text{ erg s}^{-1}$ at 0.3–75 keV and a bolometric X-ray luminosity of $(4.6 \pm 0.3) \times 10^{33} \text{ erg s}^{-1}$.

The *NuSTAR* data suggest a pronounced fluorescent iron line at 6.4 keV with an equivalent width (EW) estimated in $179^{+19}_{-61} \text{ eV}$. As we show below, this value is significantly higher than that derived for V2731 Oph with the same instrument, even though V2731 Oph is significantly more absorbed than TV Col. Thus, the fluorescent line, at least for TV Col, seems to have a contribution not only from the absorber but also from the reflector.

4.1.2. Spectral Evolution from *Swift*/XRT Observations

We investigated five other archival *Swift*/XRT observations of TV Col individually in order to evaluate its spectral evolution (Table 1). Thermal models resulted in unconstrained values for the plasma temperature and abundance, while they were consistent with those obtained from the simultaneous *NuSTAR* and *Swift* observations. Subsequently, we fitted the spectra by assuming the model M4_m, keeping the plasma temperature and abundance values of the MKCFLOW and the parameters of the REFLECT component fixed to those determined previously from the *NuSTAR*/*Swift* observations

Table 4
TV Col: Best-fit Spectral Parameters from *Swift*/XRT Observations

<i>Swift</i> /XRT (ObsID)	pwab		APEC	BBODY	$F_{\text{unabs},0.3-10\text{keV}}$ ($\times 10^{-11} \text{ erg cm}^{-2} \text{ s}^{-1}$)	$\chi^2_{\nu}/\text{d.o.f.}$
	$N_{\text{H,max}}$ (10^{22} cm^{-2})	β	kT (keV)	kT (keV)		
00035282001	$13.8^{+3.4}_{-2.1}$	$-0.41^{+0.03}_{-0.03}$	6.5	1.04/398
	$12.7^{+2.6}_{-2.7}$	$-0.38^{+0.04}_{-0.01}$	$0.14^{+0.06}_{-0.04}$...	6.7	1.04/396
	$12.7^{+3.0}_{-3.2}$	$-0.38^{+0.09}_{-0.02}$...	$0.11^{+0.06}_{-0.05}$	6.6	1.04/396
00035282002	$13.6^{+8.0}_{-5.1}$	$-0.40^{+0.09}_{-0.06}$	6.9	0.88/65
00037150002	$17.2^{+3.9}_{-1.4}$	$-0.37^{+0.02}_{-0.03}$	$0.18^{+0.01}_{-0.02}$...	8.6	1.12/689
	$15.9^{+2.1}_{-0.2}$	$-0.35^{+0.01}_{-0.02}$...	$0.12^{+0.01}_{-0.01}$	8.5	1.13/689
00037150003	$13.4^{+3.5}_{-2.9}$	$-0.35^{+0.06}_{-0.04}$	$0.18^{+0.05}_{-0.06}$...	7.8	1.01/297
	$10.1^{+4.2}_{-2.4}$	$-0.23^{+0.20}_{-0.11}$...	$0.15^{+0.02}_{-0.03}$	7.9	1.01/297
00037150005	$25.3^{+17.6}_{-5.4}$	$-0.43^{+0.02}_{-0.04}$	$0.15^{+0.03}_{-0.02}$...	11.2	1.00/389
	$31.7^{+13.6}_{-9.2}$	$-0.45^{+0.03}_{-0.03}$...	$0.09^{+0.02}_{-0.02}$	11.6	1.03/389

Note. From M4_m or M5 (see Table 2).

of 2014 May 11/12, presented in Table 3. We also adopted the same fixed parameter values as done previously for the M4_m model. The best-fit spectral parameters are summarized in Table 4.

There is an excess emission below ~ 1 keV that indicates the presence of an additional thermal component for two observations (0003715002 and 0003715005) and is suspected for two others (00035282001 and 0003715003). Its description suggests that it is more likely due to a cool, optically thin plasma ($kT \sim 0.15$ keV), but a blackbody emission ($kT \sim 0.12$ keV) cannot be ruled out. No strong change in the spectral shape of TV Col is observed in the first five *Swift* observations listed in Table 1, but they still exhibit variability in the absorbers and the unabsorbed flux at 0.3–10 keV. Remarkably, during the fifth observation, the values increased by 50%–100%.

4.2. V2731 Oph

It is clear from the investigation of TV Col that simultaneous, or at least contemporaneous, broadband coverage is essential in describing the effects of both absorption and reflection of X-rays and hence in characterizing the system. Even though V2731 Oph has been observed with high signal-to-noise ratios in soft and hard X-rays, the coverage in both energy bands with different satellites was not contemporaneous.

We started by comparing the previous *XMM-Newton* observation (carried out on 2005 August 29) already reported by de Martino et al. (2008) with the *Suzaku* (2009 February 16; Yuasa et al. 2010) and the longest *Swift* (2007 February 23) archival observations of V2731 Oph (Table 1). Those observations were investigated separately and, subsequently, via a joint fit with the 20–75 keV *NuSTAR* (2014 May 14) spectra. For the purpose of obtaining the base fit of the *XMM-Newton* data below 10 keV, we fit them jointly with the *NuSTAR* spectra restricted to the 20–75 keV range, allowing us to utilize the parameters that best describe the high-energy shape of the spectrum. In this procedure, we ignored the *NuSTAR* data below 20 keV because of our suspicion (later confirmed) that there is more spectral variability at low energies. We then proceeded with an investigation of the *NuSTAR* observations of the system separately using the whole available spectral range (3–75 keV), and then with the *Swift* and *Suzaku* spectra, also

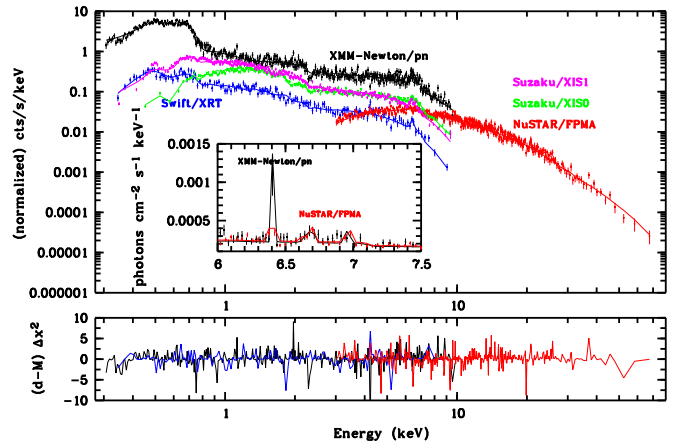


Figure 2. V2731 Oph: *XMM*/pn, *Swift*/XRT, *NuSTAR*/FPMA, *Suzaku*/XIS0, and *Suzaku*/XIS1 spectra and the corresponding descriptions from M6. The inset presents the unfolded *XMM*/pn and *NuSTAR*/FPMA data and modeling around the Fe K complex. For *Suzaku*/XIS0 and XIS1, see zoom in Figure 3.

separately, in all cases fixing the values of the cooling-flow component to those derived from the simultaneous fit of the *XMM-Newton* and the 20–75 keV *NuSTAR* spectra. Figure 2 shows the spectra.

4.2.1. Clues about the Spectral Evolution

As reported by de Martino et al. (2008), an *XMM-Newton* observation revealed a complex X-ray spectrum of V2731 Oph. A good fit required multiple thermal plasma components, with both a cold and another hot optically thin plasma, and an additional blackbody emission. Once produced, the X-rays are affected by a complex distribution of cold matter and also suffer absorption from warm material, as indicated by the O VII absorption edge at 0.74 keV. The authors showed that the spectral distribution is well explained using the model WABS*PCFABS*EDGE(MEKAL+BBODY+MEKAL+GAUSSIAN).

We first applied the model used by de Martino et al. (2008) to carry out a simultaneous fit of the three EPIC *XMM-Newton* spectra (pn, MOS1, and MOS2) and reproduced their results. However, in the following, we adopt the (updated) PHABS model instead of WABS and the (more appropriate) pwab model in the place of PCFABS. Also, we replace the APEC describing the hottest

Table 5
V2731 Oph: Best-fit Spectral Parameters

	PHABS		pwab ^a		EDGE ^b	APEC	BBODY	MKCFLOW ^c	Z^d (Z_\odot)	χ^2_ν /d.o.f.
	N_H (10^{22} cm^{-2})	$N_{H,\text{max}}$	β	Abs. Depth (@0.74 keV)	kT	kT (keV)	kT_{max}			
Without REFLECT from M6 and Its Variants										
Model: CONSTANT*PHABS*PWAB*EDGE*(APEC + MKCFLOW + BBODY + GAUSSIAN)										
<i>XMM</i> + <i>NuSTAR</i> ^e	$0.33^{+0.02}_{-0.02}$	156^{+270}_{-42}	$-0.68^{+0.01}_{-0.01}$	$1.86^{+0.08}_{-0.09}$	$0.17^{+0.01}_{-0.02}$	$0.094^{+0.002}_{-0.002}$	$47.6^{+4.2}_{-4.5}$	$0.30^{+0.09}_{-0.09}$	1.01/962	
<i>Swift</i>	$0.29^{+0.03}_{-0.03}$	156^f	$-0.75^{+0.04}_{-0.04}$	$1.46^{+0.22}_{-0.24}$	$0.64^{+0.05}_{-0.06}$	0.094^b	47.6^f	0.30^f	1.02/150	
Model: CONSTANT*PWAB*EDGE*(APEC + MKCFLOW + BBODY + GAUSSIAN)										
<i>Suzaku</i> (XIS0+3)	...	156^f	$-0.78^{+0.01}_{-0.01}$	$0.72^{+0.07}_{-0.07}$	$0.25^{+0.01}_{-0.01}$	$0.21^{+0.01}_{-0.01}$	47.6^f	0.30^f	1.06/1663	
<i>Suzaku</i> (XIS0+1+3)	...	156^f	$-0.80^{+0.01}_{-0.01}$	$0.75^{+0.04}_{-0.04}$	$0.28^{+0.01}_{-0.01}$	$0.18^{+0.01}_{-0.01}$	47.6^f	0.30^f	1.18/2574	
Model: CONSTANT*PWAB*(MKCFLOW + GAUSSIAN)										
<i>NuSTAR</i> (3–75 keV)	...	753^{+60}_{-62}	$-0.68^{+0.01}_{-0.01}$	47.6^f	0.30^f	1.00/782	
<i>NuSTAR</i> (3–75 keV)	...	766^{+131}_{-88}	$-0.68^{+0.01}_{-0.01}$	$46.7^{+3.6}_{-3.7}$	0.30^f	1.02/781	
With REFLECT from M7 and Its Variants										
Model: CONSTANT*PHABS*PWAB*EDGE*(APEC + REFLECT*MKCFLOW + BBODY + GAUSSIAN)										
<i>XMM</i> + <i>NuSTAR</i> ^e	$0.36^{+0.02}_{-0.02}$	150^{+487}_{-62}	$-0.76^{+0.01}_{-0.01}$	$1.83^{+0.09}_{-0.09}$	$0.17^{+0.01}_{-0.02}$	$0.093^{+0.002}_{-0.002}$	$54.5^{+6.4}_{-4.3}$	$0.23^{+0.07}_{-0.05}$	0.98/962	
<i>XMM</i> + <i>NuSTAR</i> ^e	$0.36^{+0.02}_{-0.02}$	121^{+135}_{-35}	$-0.76^{+0.01}_{-0.01}$	$1.83^{+0.09}_{-0.09}$	$0.17^{+0.01}_{-0.02}$	$0.092^{+0.002}_{-0.002}$	$55.1^{+6.2}_{-4.4}$	0.30^f	0.98/963	
<i>Swift</i>	$0.59^{+0.09}_{-0.11}$	121^f	$-0.93^{+0.03}_{-0.03}$	$1.28^{+0.24}_{-0.27}$	$0.22^{+0.02}_{-0.01}$	$0.04^{+0.01}_{-0.01}$	55.1^f	0.30^f	0.97/149	
Model: CONSTANT*PWAB*EDGE*(APEC + REFLECT*MKCFLOW + BBODY + GAUSSIAN)										
<i>Suzaku</i> (XIS0+3)	...	121^f	$-0.88^{+0.01}_{-0.01}$	$0.74^{+0.06}_{-0.07}$	$0.25^{+0.01}_{-0.01}$	$0.20^{+0.01}_{-0.01}$	55.1^f	0.30^f	1.05/1663	
<i>Suzaku</i> (XIS0+1+3)	...	121^f	$-0.90^{+0.01}_{-0.01}$	$0.74^{+0.04}_{-0.04}$	$0.30^{+0.01}_{-0.01}$	$0.18^{+0.01}_{-0.01}$	55.1^f	0.30^f	1.18/2574	
Model: CONSTANT*PWAB*(REFLECT*MKCFLOW + GAUSSIAN)										
<i>NuSTAR</i> (3–75 keV)	...	848^{+174}_{-167}	$-0.82^{+0.01}_{-0.01}$	55.1^f	0.30^f	0.96/782	
<i>NuSTAR</i> (3–75 keV)	...	895^{+206}_{-198}	$-0.82^{+0.01}_{-0.01}$	$55.8^{+5.3}_{-3.8}$	0.30^f	0.98/781	

Notes.^a $N_{H,\text{min}} = 10^{15} \text{ cm}^{-2}$.^b Threshold energy equal to 0.74 keV.^c $kT_{\text{low}} = 80.8 \text{ eV}$.^d Z tied to the APEC, MKCFLOW, and, when present, REFLECT components for all of the elements.^e Using only the 20–75 keV *NuSTAR* spectra (FPMA and FPMB).^f Fixed to the values of the joining *XMM* + *NuSTAR* analysis. For the REFLECT component, when applied, the reflection scaling factor is equal to 1 and $\cos(i) = 0.45$. The lack of coverage for $E < 3 \text{ keV}$ from *NuSTAR* data does not allow a reliable determination of the flux at 0.3–10 keV. For the *Suzaku* analysis, see text.

thermal component with the MKCFLOW model, in line with the case of our other target, TV Col, and as it is expected for IPs. Thus, the final model is M6: CONSTANT*PHABS*PWAB*EDGE*(MKCFLOW+APEC+BBODY+GAUSSIAN).

Model M6 describes the *XMM-Newton* data well, resulting in $\chi^2_\nu = 1.05$ for 834 degrees of freedom, but the hottest component of the MKCFLOW component converged to the hard limit of $kT = 79.9 \text{ keV}$. The coldest component, as for the case of TV Col, was not constrained and therefore fixed to $kT = 80.8 \text{ eV}$. We added to the fit the *NuSTAR* spectra limited to the 20–75 keV energy range. This inclusion improves the statistic to $\chi^2_\nu = 1.01$ for 962 degrees of freedom while resulting in well-constrained values (Table 5). Starting with the plasma parameters, the temperature derived from the MKCFLOW model peaks at $kT = 47.6^{+4.2}_{-4.5} \text{ keV}$. A cold ($kT = 0.17^{+0.01}_{-0.02} \text{ keV}$), optically thin plasma component is necessary to account for a substantial part of the ~ 0.5 – 1.5 keV range that is not described by the MKCFLOW model, even taking its low temperature as a free parameter during the fit. A fit without the cold plasma but with the low temperature left to vary free only achieves $\chi^2_\nu = 1.15$. On the other hand, we confirm that a blackbody component (with $kT = 0.094^{+0.002}_{-0.002} \text{ keV}$) is a good

description for the excess emission in soft X-rays not explained by the optically thin plasma emission. However, this is unphysical for a WD, as is argued at the end of this section. In terms of absorption, the modeling with pwab resulted in a complex structure with $N_{H,\text{max}} = 156^{+270}_{-42} \times 10^{22} \text{ cm}^{-2}$ and $\beta = -0.68^{+0.01}_{-0.01}$. Although poorly constrained, the lower limit to $N_{H,\text{max}}$ is still high: at least $\sim 10^{24} \text{ cm}^{-2}$. The $N_{H,\text{min}}$ parameter, unconstrained, was fixed to 10^{15} cm^{-2} , the minimum value allowed by the model. The PHABS resulted in the equivalent to $N_H = (3.3 \pm 0.2) \times 10^{21} \text{ cm}^{-2}$. Such a value is higher than the total Galactic HI column density in the direction of V2731 Oph of about $1.6 \times 10^{21} \text{ cm}^{-2}$ estimated by Kalberla et al. (2005) but slightly lower than the value of $3.9 \times 10^{21} \text{ cm}^{-2}$ derived from the 3D dust mapping with Pan-STARRS 1⁶ (Green et al. 2018). The abundance was tied to the APEC and MKCFLOW models, resulting in $Z = 0.30 \pm 0.09 Z_\odot$. This value is consistent with the two values reported by de Martino et al. (2008) of $0.33^{+0.37}_{-0.19} Z_\odot$ from the 0.3–10 keV *XMM-Newton* EPIC data alone and $0.40^{+0.07}_{-0.08} Z_\odot$ when the 20–100 keV *INTEGRAL*/ISGRI spectrum was also included in

⁶ <http://argonaut.skymaps.info/>

the analysis. The energy of the EDGE component was fixed at 0.74 keV (corresponding to the O VII absorption edge reported by de Martino et al. 2008).

The aim of this analysis is to compare how the spectral energy distribution has evolved when comparing observations carried out at different epochs. In this exercise, we explore the longest archival *Swift* observations and the *Suzaku* observation of V2731 Oph, verifying the consistency of the spectra with the model used to describe the 0.3–10 keV *XMM-Newton* plus the 20–75 keV *NuSTAR* spectra.

We first investigate the *Swift*/XRT spectrum (ObsID 00035086002). The model and values derived from the joint *XMM-Newton* and *NuSTAR* analysis, keeping only the normalization as free parameters, result in an unacceptable description of the *Swift* spectrum ($\chi^2_\nu = 3.18$). The statistic is slightly improved when allowing the parameter of the PHABS to vary ($\chi^2_\nu = 2.54$). There is no improvement when allowing the $N_{\text{H,max}}$ parameter of the p_{wab} model free to vary during the fit, and its value is unconstrained. On the other hand, the fit is significantly improved when the β parameter of this component is allowed to vary ($\chi^2_\nu = 1.59$), again keeping the lower limit for the absorption fixed. The statistic improves to $\chi^2_\nu = 1.14$ when the absorption depth of the EDGE component is also a free parameter. Allowing the plasma temperature of the APEC component to also vary improves the fit description ($\chi^2_\nu = 1.06$). On the other hand, there is no improvement when allowing the temperature of the BBODY component and the high-temperature parameter of the MKCFLOW model to vary. As their values are consistent with those derived from the *XMM-Newton* plus *NuSTAR* analysis, we kept them fixed to the corresponding values. The best-fit spectral parameters are summarized in Table 5. The analysis revealed a significant change in the partial-covering absorption and the temperature of the cold plasma component, while the spectral energy distribution of hard X-rays remained essentially unchanged.

We extended the same methodology to the *Suzaku* XIS0, XIS1, and XIS3 spectra. Allowing only the normalization to vary during the fit resulted in $\chi^2_\nu = 6.30$. As for the XRT spectrum, the description is improved when allowing the absorption column of the PHABS ($\chi^2_\nu = 3.70$), the β parameter of the p_{wab} model ($\chi^2_\nu = 2.34$), the absorption depth of the EDGE component ($\chi^2_\nu = 1.54$), and the plasma temperature of the APEC component ($\chi^2_\nu = 1.42$) to vary. The column derived from the PHABS model is virtually equal to zero ($N_{\text{H}} \sim 10^{16} \text{ cm}^{-2}$) and unphysical, and this component was removed without impacting the fit. The lower limit of the absorption in the PHABS converges to the minimum value when assumed as a free parameter. In contrast with the *Swift* spectrum, the fit for the *Suzaku* spectra is statistically improved when the temperature of the BBODY component is free during the fit ($kT \sim 0.18 \text{ keV}$; $\chi^2_\nu = 1.22$). Table 5 includes the best-fit parameters of the *Suzaku* observation.

However, there are four significant issues with the fit to the *Suzaku* data. First, the model underestimates the flux around 0.5 keV and also around 0.8 keV (see Figure 3). Second, the column density for the PHABS component is unrealistically low in comparison with the total Galactic HI column density in this direction ($\sim 1.6 \times 10^{21} \text{ cm}^{-2}$ according to Kalberla et al. 2005 and $3.9 \times 10^{21} \text{ cm}^{-2}$ from the 3D dust mapping with Pan-STARRS 1 by Green et al. 2018). Given the large distance to V2731 Oph (at least 2 kpc), we expect that a substantial

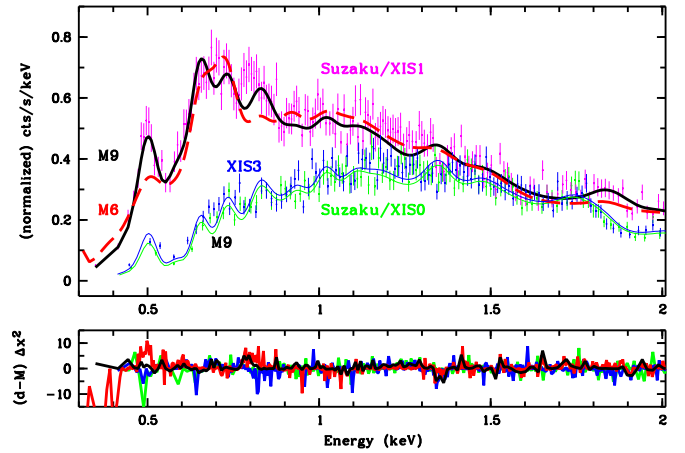


Figure 3. V2731 Oph: *Suzaku*/XIS0 and XIS3 spectra fitted with model M9 (green and blue, respectively) and *Suzaku*/XIS1 spectrum (magenta) with models M6 (red) and M9 (black), zoomed on the low-energy tail. See text for further details.

fraction of this column is between V2731 Oph and the solar system. The fact that the N_{H} for the PHABS component was negligible when fitting the *Suzaku* data, while it was higher than the Galactic value in the *XMM-Newton* and *Swift* data, points to a possible problem with the fit. Third, the blackbody temperature, already worryingly high in the *XMM-Newton* fit, is so high as to be clearly unphysical for a WD (Williams et al. 1987); we will return to this point in Section 6.1. Fourth, this model does not fit the XIS1 data, which show significant residuals below $\sim 0.8 \text{ keV}$, especially around 0.5 keV. While some cross-calibration issues among the XIS units of *Suzaku* are commonly seen, what we see in V2731 Oph is far beyond the residuals seen in other *Suzaku* observations. One likely explanation is that the model is wrong but nevertheless works well enough, phenomenologically, with *XMM-Newton*, *Swift*/XRT, and *Suzaku* XIS0+XIS3 data (Table 5). In fact, the best-fit spectral parameters from the XIS0+XIS3 data with M6 and M7-like models are similar to those obtained from the XIS0+XIS1+XIS3 data. Because the *Suzaku*/XIS1, using an advanced backside-illuminated CCD chip, has a relatively high effective area below 0.8 keV and a superior spectral resolution at these energies to those of the other cameras used in this work, some inadequacies of these models become readily visible in the XIS1 data. Thus, we explore in the next section an alternative spectral description of V2731 Oph.

4.2.2. Alternative Spectral Description

The *Suzaku*/XIS1 spectrum indicates a more pronounced excess around 0.5 keV than in other spectra, suggesting the presence of an intense N VII Ly α line (see red line from M6 in Figure 3). In order to check for an overabundance of N, we replace APEC with VAPEC and MKCFLOW with VMCFLOW and apply the model without reflection to the *Suzaku* XIS0, XIS1, and XIS3 spectra simultaneously, as the variants of the first models that allow the user to set the abundance of the main elements individually. The abundance for the VAPEC and VMCFLOW were tied together, allowing Z_{N} to vary freely during the fit but keeping all other elemental abundances equal to $0.30 Z_{\odot}$. The fit improves significantly with a better description of the soft tail (χ^2_{red} from 1.50 to 1.25; yet unacceptable and not presented). It indicates $Z_{\text{N}} = 3.2(\pm 0.3)Z_{\odot}$ while the normalization of the BBODY

Table 6
V2731 Oph: Best-fit Spectral Parameters Using VAPEC and VMCFLOW

	M8 <i>XMM + NuSTAR</i> ^a	M8 <i>Suzaku</i> (XIS0+1+3)	M9 <i>Suzaku</i> (XIS0+1+3)
PHABS			
N_{H} (10^{22} cm $^{-2}$)	$0.14^{+0.02}_{-0.02}$	<0.004	$0.29^{+0.02}_{-0.03}$
pwab ^b			
$N_{\text{H,max}}$ (10^{22} cm $^{-2}$)	612^{+183}_{-155}	374	68^{+15}_{-20}
β	$-0.63^{+0.01}_{-0.01}$	$-0.79^{+0.01}_{-0.01}$	$-0.77^{+0.02}_{-0.01}$
EDGE ^c			
Abs. depth (@0.74 keV)	$1.49^{+0.08}_{-0.08}$	$0.52^{+0.06}_{-0.05}$	$0.97^{+0.08}_{-0.06}$
VAPEC			
kT (keV)	$0.23^{+0.01}_{-0.01}$	$0.50^{+0.01}_{-0.02}$	$0.49^{+0.02}_{-0.02}$
VMCFLOW ^d			
kT_{max} (keV)	$43.4^{+5.0}_{-4.0}$	43.4^{f}	47.6^{g}
Z_{N} ($Z_{\text{N},\odot}$) ^e	$5.8^{+1.0}_{-0.7}$	$16.9^{+2.3}_{-2.1}$	69^{+16}_{-10}
Z_{O} ($Z_{\text{O},\odot}$) ^e	$0.5^{+0.1}_{-0.1}$	$1.3^{+0.2}_{-0.1}$	$4.6^{+0.8}_{-0.5}$
$Z_{\text{Fe;Ni}}$ ($Z_{\text{Fe;Ni},\odot}$) ^e	$0.37^{+0.04}_{-0.04}$	$0.19^{+0.01}_{-0.02}$	$0.6^{+0.1}_{-0.1}$
BBODY			
kT (eV)	39^{+5}_{-4}
GAUSSIAN			
Line energy (keV)	$0.58^{+0.01}_{-0.01}$
Line energy (keV)	$0.94^{+0.01}_{-0.01}$
$\chi^2_{\nu}/\text{d.o.f.}$	1.08/962	1.19/2571	1.12/2565

Notes.^a Using only the 20–75 keV *NuSTAR* spectra (FPMA and FPMB).^b $N_{\text{H,min}} = 10^{15}$ cm $^{-2}$.^c Threshold energy equal to 0.74 keV.^d $kT_{\text{low}} = 80.8$ eV.^e Z tied to the VAPEC and VMCFLOW components and fixed to 0.3 Z_{\odot} for all other elemental abundance.^f Fixed to the value of the joining *XMM + NuSTAR* analysis from M8.^g Fixed to the value of the joining *XMM + NuSTAR* analysis from M6 (in Table 5).

component tends to zero; therefore, such a component would not be necessary anymore. The PHABS N_{H} value of $7.4^{+1.0}_{-0.9} \times 10^{20}$ cm $^{-2}$ is consistent with the ISM value, while the complex absorption via pwab indicates an $N_{\text{H,max}}$ of at least 10^{24} cm $^{-2}$ with β equal to -0.90 ± 0.01 . Another difference with respect to the values inferred from the other spectra is the substantially lower absorption depth associated with the oxygen edge of 0.21 ± 0.05 . We then assumed the O abundance as a free parameter during the fit, as well as the Fe abundance, which was tied to that of Ni. The fit resulted in $Z_{\text{N}} = 16.9^{+2.3}_{-2.1} Z_{\odot}$, $Z_{\text{O}} = 1.3^{+0.2}_{-0.1} Z_{\odot}$, and $Z_{\text{Fe}} (= Z_{\text{Ni}}) = 0.19 \pm 0.02 Z_{\odot}$, with $\chi^2_{\text{red}} = 1.19$. In this scenario, the absorption from the PHABS is less than 10^{20} cm $^{-2}$, with the pwab component indicating an $N_{\text{H,max}}$ of at least 10^{24} cm $^{-2}$ and β equal to -0.79 ± 0.01 . The temperature from the VBAPEC component is $kT = 0.50^{+0.1}_{-0.2}$ keV (the kT_{max} in VMCFLOW was kept fixed to 43.4 keV, as it was derived from the *XMM+NuSTAR* for the same model). The improvement with this model comes from a better description of the continuum around 2–5 keV, but it degrades the description of the ionized iron lines around 6.7 keV and also fails to explain the X-rays in the 0.55–0.7 and 1–1.5 keV energy ranges. The addition of another thermal plasma component did not improve the fit. Again, as in

the analysis presented in Section 4.2.1, the PHABS results in a unrealistically low column density. The results are summarized in Table 6.

The model has the O VII edge at 0.74 keV, and some of the oxygen ions that absorbed such photons would emit the O VII He-like triplet. We then added a Gaussian line to the variable abundance model, and its energy centroid converged to 0.58 keV, the expected value of the O VII triplet. It results in $\chi^2_{\nu} = 1.15$, but this time not only with low column density from the PHABS component but also underestimating the spectra below 0.6 keV. We then added the BBODY component, resulting in a better description. The continuum below 0.6 keV is well described, the column density from PHABS converges to $\sim 3.8 \times 10^{21}$ cm $^{-2}$, and the temperature of the BBODY, contrary to the model presented in Section 4.2.1, has a low temperature of ~ 28 eV but an unrealistic normalization of 2.5. The χ^2_{ν} is 1.16.

Because of the excess observed around 0.90–0.94 keV, which is consistent with the position of the Ne IX triplet, we add a new Gaussian component. The centroid energies of the Gaussian lines converge to 0.58 ± 0.01 and 0.94 ± 0.01 keV, in good agreement with what is expected for the O VII and Ne IX He-like triplets, respectively. For the blackbody

component, we derive $kT = 39^{+5}_{-4}$ eV and a normalization of $(4.3^{+4.0}_{-2.4}) \times 10^{-2}$. The column from the PHABS component is $2.9^{+0.2}_{-0.3} \times 10^{21}$ cm⁻², consistent with the value expected from the ISM in the light of sight of V2731 Oph. The fit also results in $N_{\text{H,max}} = 68^{+15}_{-20} \times 10^{22}$ cm⁻² and $\beta = -0.77^{+0.02}_{-0.01}$ for pwab and $kT = 0.49 \pm 0.02$ keV for VAPEC. For the VMCFLOW component, we kept $kT_{\text{max}} = 47.6$ keV. Also, the fit, with $\chi^2_{\nu} = 1.12$, resulted in $Z_{\text{N}} = 69^{+16}_{-10} Z_{\odot}$, $Z_{\text{O}} = 4.6^{+0.8}_{-0.5} Z_{\odot}$, and $Z_{\text{Fe}} (= Z_{\text{Ni}}) = 0.6^{+0.1}_{-0.1} Z_{\odot}$. The best-fit spectral parameters are presented in Table 6. In Figure 3, we present the fits from M6 and M9 for *Suzaku*/XIS1 (red and black lines, respectively), where we also present the XIS0 and XIS3 spectra and the corresponding results from M9.

We applied the above models to the *XMM-Newton* EPIC spectra. The fit with variable Z_{N} was found to be statistically worse than the previous description using model M6 (Table 5), with a χ^2_{ν} of 1.14. When both Z_{N} and Z_{O} are allowed to be free, without the O absorption edge, it results in difficulties in explaining the emission from 0.7 to 0.8 keV. Finally, we applied M8 (see Table 2) to the combined *XMM-Newton* and 20–75 keV *NuSTAR* data and obtained a χ^2_{ν} of 1.08 (compared to 1.01 for M6) with similar parameter values when exploring only the *XMM-Newton* spectra, particularly kT_{max} , which shows no statistically significant changes. The results are shown in Table 6. The addition of a BBODY and the two GAUSSIAN lines as in M9 does not improve the fit. With a low temperature ($kT \sim 15$ eV), the BBODY component converges to a normalization of only $\sim 10^{-19}$, meaning that such an addition is not supported by the data. A GAUSSIAN component at 0.94 keV, as applied to the *Suzaku* data, is not constrained by the fit, and fixing its parameters to the values derived from the *Suzaku* spectra does not improve the fit. Also, although still in agreement with the *XMM-Newton* data, the GAUSSIAN line around 0.58 keV results in no significant improvement in the fit, still with a χ^2_{ν} of 1.08. The values derived from M8 (Table 6) are mutually consistent with those when applying M9 to the 0.3–10 keV *XMM-Newton* plus the 20–75 keV *NuSTAR* spectra, although these fits are not shown.

Thus, even though we have not found a completely satisfactory fit to the soft X-ray spectrum, our idea to combine *XMM-Newton* and 20–75 keV *NuSTAR* data appears to be valid. First, the spectral energy distributions for hard X-rays in both sets of data are mutually consistent and confirmed from the whole spectral range covered by *NuSTAR* (Section 4.2.3). The difficulties with either model in describing the *Suzaku* data with all applied models and the *XMM-Newton* spectra with the alternative M8 and M9 models are limited to the soft end of the spectrum (<1 keV). We notice that the elemental abundances derived independently from the *Suzaku* and *XMM-Newton* spectra do not converge; both indicate that anomalies are present, at least for the N, O, and Fe. Second, the absorbed and unabsorbed 20–75 keV fluxes differ by less than 5%, showing that the absorption such as detected in the system, even though it is very high, has no significant role in this spectral region. In addition, the investigation revealed that the luminosity of the source at 20–75 keV during the *XMM-Newton* observation is $\sim 35\%$ less than that observed during the *NuSTAR* observation, with the unabsorbed flux varying from $\sim 2.5 \times 10^{-11}$ to $\sim 3.9 \times 10^{-11}$ erg cm⁻² s⁻¹ (over 9 yr). The estimated unabsorbed 20–75 keV flux from both the *Swift* and *Suzaku* data sets is $\sim 2.1 \times 10^{-11}$ erg cm⁻² s⁻¹ (over 2 yr). Since the soft X-ray complexity is limited to energies below 0.8 keV, we will

proceed by returning to the spectral model of de Martino et al. (2008) in the analysis of hard X-ray data and comment on the soft X-ray complexity in Section 6.1.

4.2.3. Spectroscopy Using the Full *NuSTAR* Data

The variability of V2731 Oph in X-rays prevents the use of noncontemporaneous campaigns to carry out a simultaneous spectral fit. Therefore, we instead explored the full spectral range covered by *NuSTAR* (3–75 keV) initially using model M6. As expected, the PHABS (that goes virtually to zero; $N_{\text{H}} = 10^{13}$ cm⁻²), BBODY, APEC, and EDGE components do not contribute to the fit, and they were removed from the model. A fit that keeps the $N_{\text{H,max}}$ of the pwab component fixed to 156×10^{22} cm⁻² and the kT_{hot} of the MKCFLOW to 47.6 keV, as derived from the analysis of the *XMM-Newton* and 20–50 keV *NuSTAR* spectra, yields $\chi^2_{\nu} = 1.48$. Freezing the thermal component to 47.6 keV and allowing the $N_{\text{H,max}}$ to vary during the fit results in a good description of the spectra with $N_{\text{H,max}} = 753^{+60}_{-62} \times 10^{22}$ cm⁻² and $\beta = -0.68^{+0.01}_{-0.01}$ for $\chi^2_{\nu} = 1.00$ (Table 5). The abundance was kept fixed to $0.30 Z_{\odot}$. Similar values were obtained when allowing the high temperature of the MKCFLOW to vary during the fit. The kT_{max} of $47.6^{+4.2}_{-4.5}$ keV derived from the joint *NuSTAR*/*XMM-Newton* fit suggests a WD mass of $0.92 \pm 0.04 M_{\odot}$, if the shock temperature reflects the gravitational potential just above the WD surface (following Aizu 1973).

4.2.4. Investigating the Hypothesis of Reflection

We move back to the spectral investigation of V2731 Oph to verify how the occurrence of X-ray reflection in the system would affect the results. Contrary to the case of TV Col, it was not possible to constrain the reflection—if it is present—for V2731 Oph. Adding the REFLECT component and allowing the reflection scaling factor to vary during the fits resulted, systematically, in values greater than 3, which are unrealistic. We froze this value to 1 while keeping $\cos i = 0.45$ to see how this conservative assumption would impact the spectral results when reflection is present. In doing this, we followed the same procedure as in the case without REFLECT: we investigated the EPIC *XMM-Newton* and 20–75 keV *NuSTAR* (FPMA + FPMB) simultaneously, then individually investigated the *Swift*/XRT, *Suzaku* (XIS0+XIS3 and XIS0+XIS1+XIS3), and 3–75 keV *NuSTAR* spectra. The results are summarized in Table 5. The kT_{max} of $55.1^{+6.2}_{-4.4}$ keV derived from the joint *NuSTAR*/*XMM-Newton* fit (with the abundance fixed to $0.3 Z_{\odot}$) suggests a WD mass of $0.99^{+0.05}_{-0.03} M_{\odot}$, if the shock temperature reflects the gravitational potential just above the WD surface.

The inclusion of reflection does not change the high temperature in the MKCFLOW model at the 1σ level. But this result can be masked by effects of the photoelectric absorption that is not well constrained from the *NuSTAR* data alone. A conclusive investigation of reflection in V2731 Oph demands high signal-to-noise spectroscopy covering at least the 0.3–75 keV energy range. High-resolution spectroscopy would play a crucial role in the description of the lines in the soft X-rays and therefore the continuum and, finally, the intervening absorber. As of now, our results suggest that 35% of the total flux at 10–50 keV derived for V2731 Oph from the *XMM-Newton* fit can be due to reflection—similar to the fraction inferred for TV Col, in which the presence of reflection is clear.

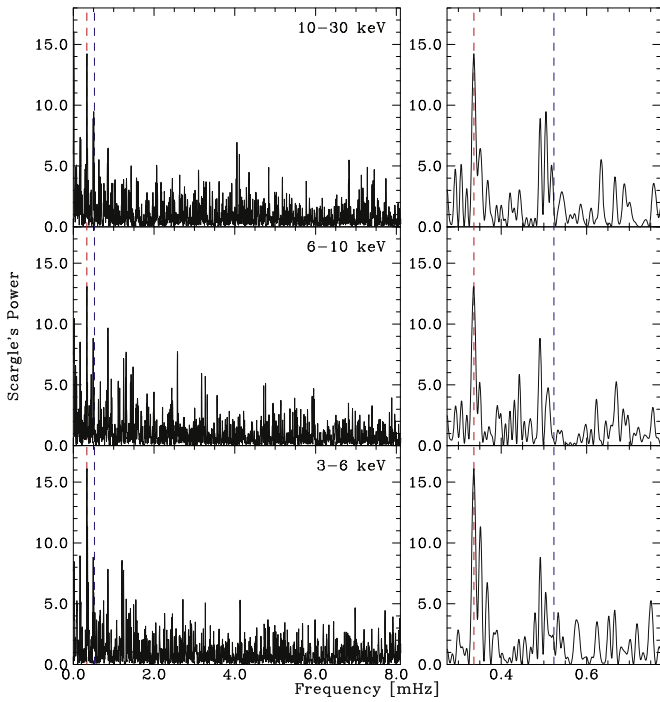


Figure 4. TV Col: periodogram from *NuSTAR* data in three X-ray energy bands: 3–6 (bottom), 6–10 (middle) and 10–30 keV (top). The set of panels show the power spectra over the range of periods we investigated (longer than 120 s). The blue dashed line is drawn at the known spin period of TV Col, 1909.7 s, while the red dashed line indicates the prominent peak at 2976 s. The right set of panels shows the power spectra around 1909.7 s in more detail.

From the *XMM-Newton* (pn; on 2005 August 29) observation, we estimate an EW of 145 ± 40 eV for the fluorescent iron line at 6.4 keV. The *NuSTAR* data have a poorer spectral resolution but suggest a lower value on 2014 May 14 of about 69 eV, even in a situation in which X-rays seem to be more absorbed than they were during the *XMM-Newton* observation (Figure 2, inset). Perhaps the low EW suggests that the 6.4 keV line can be accounted for only by the absorbers with only a small contribution, if any, from reflection.

4.2.5. X-Ray Luminosity and Mass Accretion Rate

V2731 Oph is a luminous IP in the X-rays, with a high mass accretion rate. Here we concentrate on results from the *XMM-Newton* and *NuSTAR* analyses. From the cooling-flow model, we infer directly from its normalization parameter value that the mass accretion rate during the *XMM-Newton* observation (2005 August 29) was $5.1_{-0.7}^{+2.7} \times 10^{-9} M_{\odot} \text{ yr}^{-1}$, with a bolometric luminosity of $4.2 \times 10^{35} (d/2300 \text{ pc})^2 \text{ erg s}^{-1}$, while the rate during the *NuSTAR* observation (2014 May 14) was $(8.4 \pm 0.2) \times 10^{-9} M_{\odot} \text{ yr}^{-1}$. Because *NuSTAR* does not cover energies below 3 keV, where the system has a significant contribution from additional components that are therefore not constrained from those data, we cannot infer the X-ray bolometric luminosity securely from the *NuSTAR* data. To carry out a more realistic comparison, we adopt the luminosity in the 3–75 keV band. The values are $4.4 \times 10^{34} (d/2300 \text{ pc})^2$ and $7.8 \times 10^{34} (d/2300 \text{ pc})^2 \text{ erg s}^{-1}$ for the *XMM-Newton* and *NuSTAR* observations, respectively. We estimate that the 3–75 keV luminosity is about 10% less than the bolometric X-ray luminosity.

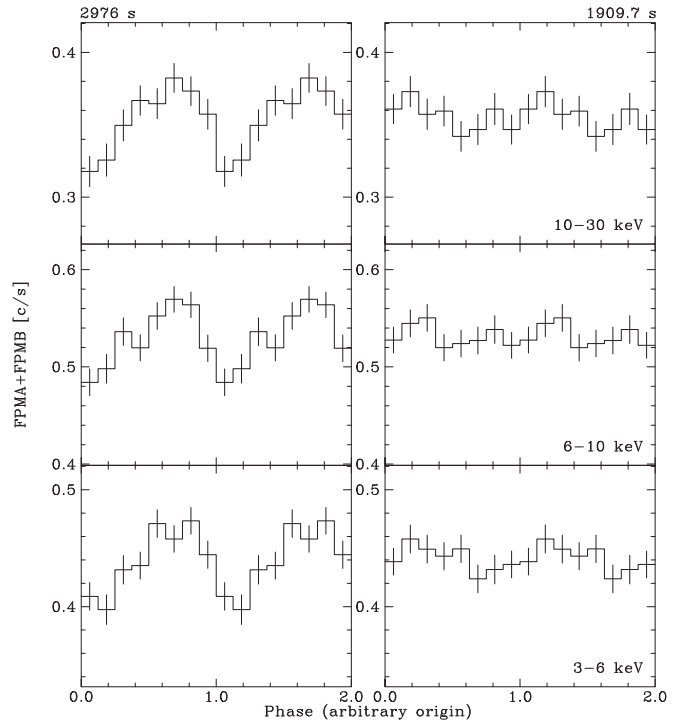


Figure 5. TV Col: Folded light curves (on the prominent period of 2976 s, left, and the known spin period of 1909.7 s, right) from *NuSTAR* data in three X-ray energy bands: 3–6 (bottom), 6–10 (middle), and 10–30 keV (top).

5. Timing Properties from the *NuSTAR* Observations

The *NuSTAR* observations allowed us to investigate the spin variability of both TV Col and V2731 Oph in hard X-rays. We proceeded from background-subtracted light curves in three energy bands: 3–6, 6–10, and 10–30 keV. We chose 60 s bins for TV Col, given its long spin period (resulting in 32 bins per cycle), and 10 s bins for V2731 Oph, given its short period (13 bins per cycle). Since the *NuSTAR* count rates of these IPs are modest, we neglected dead-time correction, which should be small. We also neglected barycentric correction to simplify the analysis procedure, since we intended to limit our analysis to the times of the *NuSTAR* observations. We combined the FPMA and FPMB light curves in the three bands and searched for periodic modulations using the Fourier power spectrum and the normalization according to Scargle (1982). There are no *Swift* data at the time of the *NuSTAR* observation of V2731 Oph, while that contemporaneous with the *NuSTAR* observation of TV Col is too short to provide conclusive results. As a timing analysis of all archival X-ray data is beyond the scope of our work, and given that an extensive body of work already exists in print, we focus on the *NuSTAR* observations.

5.1. TV Col

The known spin modulation in TV Col, refined by Rana et al. (2004) as 1909.7 ± 2.5 s, was not detected in the *NuSTAR* data. Figure 4 shows the power spectra up to 8 mHz from the three energy ranges cited above, where the blue dashed lines mark the position of the expected spin frequency. The red dashed lines in the figure mark the highest peak below 10 keV, at ~ 2976 s, while it is the second in power in the 10–30 keV energy range after the one at very low frequency ($\sim 96,000$ s). The peak at 2976 s is statistically significant if white (i.e., frequency-independent) noise is assumed. However,

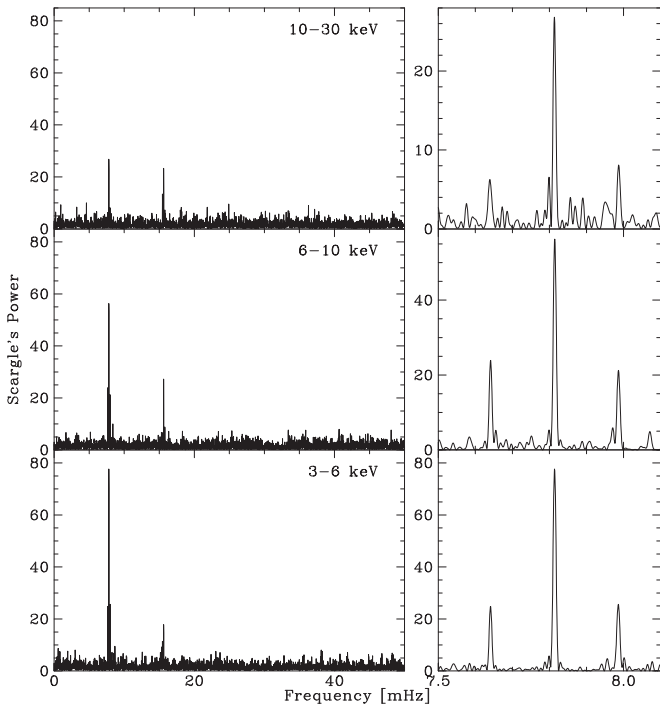


Figure 6. V2731 Oph: Periodogram from *NuSTAR* data in three X-ray energy bands: 3–6 (bottom), 6–10 (middle), and 10–30 keV (top). The set of panels show the power spectra over the range of periods we investigated (longer than 20 s). The right set of panels show the power spectra around 128 s in more detail (note the different vertical scales).

no previous reports of an ~ 3000 s period exist, so we consider this to be a noise peak.

We show folded light curves with periods of 1909 and 2976 s in the right and left panels of Figure 5, respectively. As anticipated from the power spectrum, no modulation is associated with the spin period. Using amplitude/average convention, the relative modulation amplitudes for the 2976 s peak are $\sim 7.5\%$ (3–6 keV), $\sim 6.6\%$ (6–10 keV), and 8.4% (10–30 keV), and they can be taken as conservative upper limits of the spin (1909.7 s) signal. In comparison, Rana et al. (2004) found spin amplitudes of 14% (2–5 keV), 8.5% (5–10 keV), and 6% (10–20 keV). Such modulations would have been detectable in the *NuSTAR* data below 10 keV, if not above. Thus, we conclude that the X-ray spin amplitude of TV Col is variable and that we caught it in a low spin modulation state. We note that optical observations of TV Col have long indicated a variable spin modulation amplitude (see, e.g., Bonnet-Bidaud et al. 1985; Barrett et al. 1988).

5.2. V2731 Oph

The 128 s spin period of V2731 Oph (de Martino et al. 2008) and the first harmonic are clearly dominant in the periodogram presented in Figure 6. The left panels show the periodogram over the entire frequency range (0–50 mHz, from the light curves with a time bin of 10 s) in the three X-ray energy bands under investigation. All three left panels have the same Y scale. The right panels show the expanded view around the fundamental frequency (with variable Y scales), where the peak corresponding to the 128 s period is seen with its two one-cycle-per-spacecraft-orbit aliases. The spin period for V2731 Oph is estimated to be 127.981 ± 0.022 s during the *NuSTAR* observation, consistent with the previous determination in the optical (e.g., $127.999909(49)$ s;

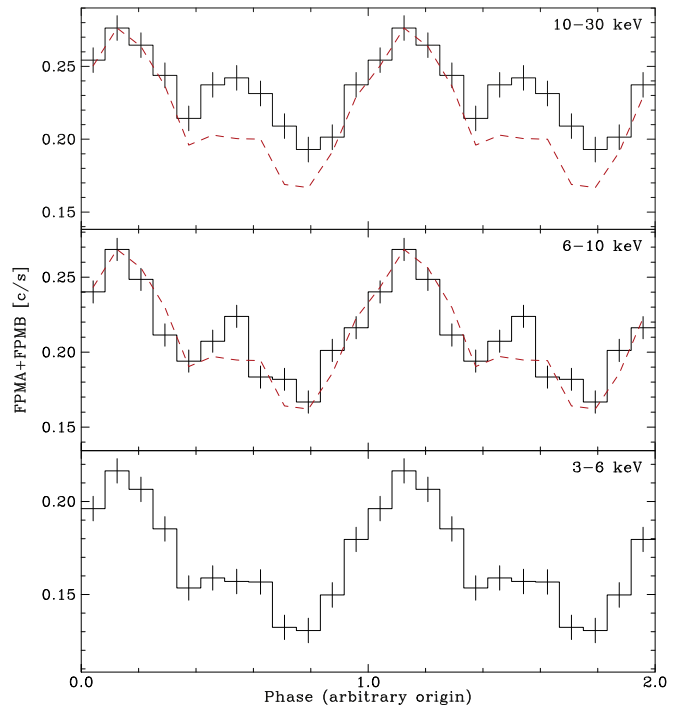


Figure 7. V2731 Oph: Light curves folded on the 127.98 s spin period from *NuSTAR* data in three X-ray energy bands: 3–6 (bottom), 6–10 (middle), and 10–30 keV (top).

Gänsicke et al. 2005) and X-rays (e.g., 128.02 ± 0.02 s; de Martino et al. 2008).

The folded light curves are not quite sinusoidal, although they are mostly so in the 3–6 keV range (Figure 7). The red dashed lines in the top and middle panels are copies of the 3–6 keV spin profile, showing that the main peak remained the same, but a secondary peak is very pronounced in the 10–30 keV range.

6. Discussion

6.1. Soft X-Ray Complexity of V2731 Oph

The fact that V2731 Oph has a complex X-ray emission was already reported by de Martino et al. (2008). Our analysis shows that their model cannot fit the *Suzaku* XIS1 spectrum. Moreover, blackbody temperatures of 0.21 and 0.18 keV, as derived from *Suzaku* XIS0+XIS3 and XIS0+XIS1+XIS3 spectra, respectively, are clearly unphysical for WD accretion. Considering the local Eddington limit, the highest effective temperature for a blackbody contribution would be ~ 140 eV for a $1.4 M_{\odot}$ WD (Williams et al. 1987), which would imply a shock temperature kT_{\max} of 230 keV. Even the 94 eV temperature, as derived from *XMM-Newton* data and consistent with *Swift* observations, demands a WD mass of at least $1.2 M_{\odot}$, with a high specific accretion rate of about $200 \text{ g cm}^{-2} \text{ s}^{-1}$ and $kT_{\max} > 100$ keV and therefore inconsistent with our spectral analysis.

Based on the *Suzaku* XIS1 spectrum, we have proposed an alternative spectral model that does not include a hot blackbody. For other instruments, but still acceptable for the *Suzaku* XIS0 and XIS3 spectra, this model results in a poorer fit than was obtained with the model with a blackbody. One plausible explanation is the limitation of the `pwab` model. While this model is the most sophisticated in terms of reproducing the

likely distribution of the number of lines of sight as a function of N_{H} (Done & Magdziarz 1998), it assumes that the absorber has the solar abundance and is not ionized. If the emitting plasma is overabundant in nitrogen, so, too, should the absorbing plasma, which is not currently taken into account. Moreover, the presence of the O VII edge means that the latter assumption is invalid. We currently model this using an edge model in addition to p_{wab} , but we believe this is not the correct model for this situation. In reality, the absorption below 0.78 keV should be less than what p_{wab} predicts, because the complex absorber is ionized and mostly transparent at these energies. We therefore believe that the current inadequacies of the model is the likely explanation for the imperfect fit. It is likely that high-resolution, high signal-to-noise X-ray spectroscopy combined with an improved grid of models would be needed to see if the alternative spectral description is correct. In the meantime, the abundance of N should be investigated using optical and UV spectroscopy. Nitrogen overabundance has been seen in a number of CVs, both magnetic and nonmagnetic (see, e.g., Gänsicke et al. 2003; Froning et al. 2012), and indicates the presence of CNO-processed matter in the system. This, in turn, can be either due to prior nuclear evolution of the donor (Schenker et al. 2002) or pollution by previous nova eruptions (Marks & Sarna 1998).

For the main purposes of this work, the exercise we carried out by using three sets of X-ray observations for V2731 Oph shows that (i) while there is no significant evidence of change in the spectral distribution of the hottest thermal component, its luminosity is variable, and its X-ray photons suffer the effect of a variable absorbing column; (ii) the hottest thermal component is in agreement with a cooling-flow, stratified multithermal model, which is expected for IP systems; and (iii) the soft X-ray spectrum is variable in flux and spectral distribution. Given these findings, we believe our results are robust regarding the complex absorber, reflection amplitude, and maximum temperature of the post-shock region, despite our imperfect understanding of the soft (<1 keV) spectrum of V2731 Oph.

6.2. Clues from the Plasma Temperature and Reflection Amplitude

While the maximum temperature (kT_{max}) derived from the MKCFLOW model traces the gravitational potential well at the accretion column shock, the reflection amplitude (Ω_r) depends on the shock height (h) with respect to the stellar surface. Thus, these two spectral signatures allow us to put constraints on the WD mass and the accretion geometry of the system.

For a pointlike emission region placed at height h above the WD, with h expressed as a fraction of the stellar radius, the stellar surface covers the solid angle (see Figure 2 of Tsujimoto et al. 2018):

$$\Omega = 2\pi(1 - \sqrt{1 - 1/(1 + h)^2}). \quad (1)$$

The reflection amplitude is defined as the solid angle covered by the reflector as seen from the emitter in such a way that it is 1.0 when the solid angle subtended is 2π (half the sky). This condition corresponds to $h = 0$ in Equation (1), and therefore $\Omega_r \equiv \Omega/2\pi$. Thus, a reflection amplitude of 0.88 ± 0.13 as derived from the spectral fit of TV Col (see Table 3) requires h of order 0.7% of the WD radius. Such a small shock height implies that kT_{max} traces the gravitational potential well virtually at the WD surface, and therefore the WD mass

determined from our spectral fit ($0.735 \pm 0.015 M_{\odot}$) does not require additional corrections.

On the other hand, as first derived by Aizu (1973), the geometrical parameter h is physically determined by the post-shock cooling time (t_c) that defines the remaining time for the accreted material to settle onto the WD. Higher density (ρ) in the accretion column accelerates the cooling ($t_c \propto 1/\rho$), resulting in smaller h . Thus, h is a function of WD mass and specific (or per unit area) accretion rate ($\text{g s}^{-1} \text{cm}^{-2}$).

Following Aizu (1973), the low h derived from the reflection in TV Col ($\sim 0.7\%$) is due to a high specific accretion rate, of order $15 \text{ g s}^{-1} \text{cm}^{-2}$. Comparing the specific accretion rate with the mass accretion rate derived from the MKCFLOW model of $(3.8 \pm 0.2) \times 10^{-10} M_{\odot} \text{ yr}^{-1}$, we estimate that the fractional area over which accretion happens (f) is about 0.02% for TV Col: a relatively high specific accretion rate and a small accretion spot. The best estimate for the spot size in IPs is that for XY Ari, for which Hellier (1997) used the X-ray eclipses to arrive at an estimate of <0.002 . If reliable determination of reflection amplitude becomes routine, there is a potential to repeat the kind of analysis we have performed for TV Col to estimate the spot sizes of IPs. This might allow future researchers to perform a statistical study against other system parameters.

On the other hand, we did not detect an unambiguous sign of reflection in the *NuSTAR* observation of V2731 Oph. Thus, we are unable to derive the specific accretion rate or the shock height in V2731 Oph from its X-ray spectrum.

6.3. Additional Constraints from the Photometry

The X-ray spin modulation of IPs is usually due to complex absorption (Norton & Watson 1989), which is not expected to produce significant spin modulation above 10 keV. Therefore, when spin modulation is seen above 10 keV, a geometrical explanation is required. A likely scenario is that nonnegligible shock height ($h > 0.1$) results in both poles being visible over a range of viewing geometry (de Martino et al. 2001).

The lack of detectable spin modulation in the *NuSTAR* data on TV Col can be explained as follows. First, we do not expect geometrical spin modulation because the shock in TV Col is very close to the stellar surface ($h \sim 0.7\%$). Second, the maximum energy at which we can detect X-ray spin modulation due to complex absorption depends on $N_{\text{H,max}}$. Our spectral fit shows $N_{\text{H,max}}$ of only $\sim 10^{23} \text{ cm}^{-2}$ during the *NuSTAR* observation, so the effects of complex absorption are mostly confined to photon energies below ~ 3 keV. The complex absorption appears to be variable from epoch to epoch according to our analysis of the *Swift* data, which also extends to lower energies. However, these *Swift* data do not have sufficient spin phase coverage, and our timing analysis was inconclusive. We expect that X-ray observations that showed spin modulations above 3 keV were obtained when TV Col was in a higher $N_{\text{H,max}}$ state.

In V2731 Oph, $N_{\text{H,max}}$ is high, so the low-energy (<10 keV) spin modulation may well have a contribution due to complex absorption. Nevertheless, the clear detection of the spin period above 10 keV (Figure 6) implies a strong geometrical component to the X-ray spin modulation in this IP. This indicates a nonnegligible shock height for V2731 Oph. We thus expect a low reflection amplitude, which can explain the absence of evidence of reflection in the X-ray spectrum of the

system. In that sense, V2731 Oph appears similar to V709 Cas (Mukai et al. 2015).

At first sight, it might seem surprising that a system as luminous as V2731 Oph should have a nonnegligible shock height h . We suggest two factors that may explain the large h . First, recall that h is determined not by the total accretion rate but by the specific accretion rate. We can explain the nonnegligible h by invoking a large f . A major factor controlling f is the pinching by the dipole magnetic field ($B \propto r^3$), the degree of which is determined by the magnetospheric radius. If we assume an approximate spin equilibrium, V2731 Oph ($P_{\text{spin}} = 128$ s) must have a much smaller magnetosphere than TV Col ($P_{\text{spin}} = 1909.07$ s), so dipole pinching is much less effective. Second, V2731 Oph may well have a massive WD. The freefall velocity is higher, which reduces the post-shock density, which reduces the X-ray cooling efficiency. Since the post-shock temperature is also high, this increases t_e , and hence h .

6.4. Our Targets and the Standard Evolutionary Scenario

The mass transfer in CVs with orbital periods less than ~ 10 hr is driven by angular momentum loss and expected to be of order $(3-5) \times 10^{-9} M_{\odot} \text{ yr}^{-1}$ for a 5.5 hr period CV, as appropriate for TV Col (Knigge et al. 2011). Both the normalization of the MKCFLOW model and the bolometric X-ray luminosity of TV Col suggest a lower accretion rate, unless a large amount of transferred material is not accreted and is lost, perhaps propelled out of the system, therefore reducing the expected accretion rate and consequent X-ray emission. The observed X-ray luminosity is typical of IPs (Schwope 2018).

This standard evolutionary scenario does not apply to V2731 Oph, so we have no quantitative prediction for the mass transfer rate in this system. The BAT-band luminosity of V2731 Oph is already $\log L_X(\text{erg s}^{-1}) = 34.6$ (Schwope 2018), the highest of all IPs, and the uncertain evolutionary driver must be capable of sustaining a high mass transfer rate. The overabundance of N , if confirmed, would place V2731 Oph among the subset of CVs known to be overabundant in N (see, e.g., Gänsicke et al. 2003). This would imply that the donor matter has been CNO-processed: the secondary of V2731 Oph may be evolved in the normal (single-star evolution) sense, or it may indicate that this is a post-thermal timescale mass transfer system (Schenker et al. 2002).

6.5. WD Masses

We have shown that both a complex absorber and reflection are necessary to fit the wideband X-ray spectrum of TV Col. The combined *NuSTAR*+*Swift* data allowed us to constrain both, as well as the maximum temperature of the X-ray-emitting plasma. The high reflection amplitude supporting a small shock height h and the long spin period indicate that the inner radius of the truncated disk is large. Taking the maximum plasma temperature as a measure of the gravitational potential just above the WD surface, we determine the WD mass to be $0.735 \pm 0.015 M_{\odot}$. Our value is somewhat smaller than but consistent with the previous *NuSTAR* measurement by Hailey et al. (2016).

On the other hand, we were unable to constrain the reflection amplitude in V2731 Oph. This has several effects on the mass measurement. First, our derived values for kT_{max} depend on

whether we include reflection (with amplitude fixed to 1.0) or not. Also, our values, particularly in the case without reflection ($0.92 \pm 0.04 M_{\odot}$), are significantly lower than what Hailey et al. (2016) derived; the reason for this is unclear. Moreover, we were unable to constrain the shock height, but the high-energy (>10 keV) spin modulation suggests it is not small. Because of this, and because V2731 Oph is a fast rotator that probably requires correction for the small inner radius of the disk, we consider our numbers to be lower limits for the true WD mass in this system.

7. Summary

We have combined analyses of broadband X-ray spectroscopy and photometry, as in Mukai et al. (2015), to study two IPs, TV Col and V2731 Oph, already analyzed by Hailey et al. (2016). We have gained valuable insight into the geometry and physics of accretion in these systems.

1. TV Col:

- (a) Complex absorption, such as described by the *pwab* model, is required to obtain a good spectral fit.
- (b) Reflection is also clearly detected, with an amplitude of 0.88 ± 0.13 , indicating a small shock height caused by a high specific accretion rate.
- (c) We do not detect the spin modulation in the *NuSTAR* data, showing that the amplitude of the spin modulation can vary over different epochs, as is also seen at optical wavelengths.
- (d) The WD mass is determined to be $0.735 \pm 0.015 M_{\odot}$.

2. V2731 Oph:

- (a) The X-ray spectrum is affected by a complex and variable local absorption, with a much higher N_{H} than for TV Col.
- (b) The spectral model, which includes a hot blackbody, used to fit the *XMM-Newton* data does not work for the *Suzaku* XIS1 data. We have tentatively proposed an alternative model without such a blackbody but with an overabundance of nitrogen.
- (c) The *NuSTAR* data did not allow us to constrain the reflection amplitude. The detection of high-energy (>10 keV) spin modulation suggests a tall shock.
- (d) A combination of clues points to a high-mass WD in V2731 Oph.

We thank the anonymous referee for numerous helpful suggestions. R.L.O. was partially supported by the Brazilian agency CNPq (Universal grants 459553/2014-3, PQ 302037/2015-2, and PDE 200289/2017-9). This work has made use of data from the European Space Agency (ESA) mission *Gaia* (<https://www.cosmos.esa.int/gaia>), processed by the *Gaia* Data Processing and Analysis Consortium (DPAC; <https://www.cosmos.esa.int/web/gaia/dpac/consortium>). Funding for the DPAC has been provided by national institutions, in particular the institutions participating in the *Gaia* Multilateral Agreement. This research has made use of the *NuSTAR* Data Analysis Software (NuSTARDAS), jointly developed by the ASI Science Data Center (ASDC, Italy) and the California Institute of Technology (Caltech, USA). This research has made use of the XRT Data Analysis Software (XRTDAS) developed under the responsibility of the ASI Science Data Center (ASDC), Italy.

Facilities: *NuSTAR*, *Swift*, *Suzaku*, *XMM-Newton*.

ORCID iDs

R. Lopes de Oliveira  <https://orcid.org/0000-0002-6211-7226>

K. Mukai  <https://orcid.org/0000-0002-8286-8094>

References

- Aizu, K. 1973, *PTPh*, **49**, 1184
- Asplund, M., Grevesse, N., Sauval, A. J., & Scott, P. 2009, *ARA&A*, **47**, 481
- Barrett, P., O'Donoghue, D., & Warner, B. 1988, *MNRAS*, **233**, 759
- Bonnet-Bidaud, J. M., Motch, C., & Mouchet, M. 1985, *A&A*, **143**, 313
- Brunschweiler, J., Greiner, J., Ajello, M., & Osborne, J. 2009, *A&A*, **496**, 121
- Cooke, B. A., Ricketts, M. J., Maccacaro, T., et al. 1978, *MNRAS*, **182**, 489
- de Martino, D., Matt, G., Mukai, K., et al. 2001, *A&A*, **377**, 499
- de Martino, D., Matt, G., Mukai, K., et al. 2008, *A&A*, **481**, 149
- Done, C., & Magdziarz, P. 1998, *MNRAS*, **298**, 737
- Froning, C. S., Long, K. S., Gänsicke, B., & Szkody, P. 2012, *ApJS*, **199**, 7
- Gaia Collaboration, Brown, A. G. A., Vallenari, A., et al. 2018, *A&A*, **616**, A1
- Gaia Collaboration, Prusti, T., de Bruijne, J. H. J., et al. 2016, *A&A*, **595**, A1
- Gänsicke, B. T., Marsh, T. R., Edge, A., et al. 2005, *MNRAS*, **361**, 141
- Gänsicke, B. T., Szkody, P., de Martino, D., et al. 2003, *ApJ*, **594**, 443
- Green, G. M., Schlafly, E. F., Finkbeiner, D., et al. 2018, *MNRAS*, **478**, 651
- Hailey, C. J., Mori, K., Perez, K., et al. 2016, *ApJ*, **826**, 160
- Hellier, C. 1997, *MNRAS*, **291**, 71
- Kalberla, P. M. W., Burton, W. B., Hartmann, D., et al. 2005, *A&A*, **440**, 775
- Knigge, C., Baraffe, I., & Patterson, J. 2011, *ApJS*, **194**, 28
- Marks, P. B., & Sarna, M. J. 1998, *MNRAS*, **301**, 699
- Mukai, K., Rana, V., Bernardini, F., & de Martino, D. 2015, *ApJL*, **807**, L30
- Norton, A. J., & Watson, M. G. 1989, *MNRAS*, **237**, 853
- Pretorius, M. L., & Mukai, K. 2014, *MNRAS*, **442**, 2580
- Rana, V. R., Singh, K. P., Schlegel, E. M., & Barrett, P. 2004, *AJ*, **127**, 489
- Scargle, J. D. 1982, *ApJ*, **263**, 835
- Schenker, K., King, A. R., Kolb, U., Wynn, G. A., & Zhang, Z. 2002, *MNRAS*, **337**, 1105
- Schrijver, J., Brinkman, A. C., & van der Woerd, H. 1987, *Ap&SS*, **130**, 261
- Schwope, A. D. 2018, *A&A*, **619**, A62
- Shaw, A. W., Heinke, C. O., Mukai, K., et al. 2018, *MNRAS*, **476**, 554
- Suleimanov, V., Revnivtsev, M., & Ritter, H. 2005, *A&A*, **435**, 191
- Suleimanov, V. F., Doroshenko, V., & Werner, K. 2019, *MNRAS*, **482**, 3622
- Tsujimoto, M., Morihana, K., Hayashi, T., & Kitaguchi, T. 2018, *PASJ*, **70**, 109
- Williams, G. A., King, A. R., & Brooker, J. R. E. 1987, *MNRAS*, **226**, 725
- Yuasa, T., Nakazawa, K., Makishima, K., et al. 2010, *A&A*, **520**, A25